© 2025 Hefei Institutes of Physical Science, Chinese Academy of Sciences and IOP Publishing.

Plasma Sci. Technol. **27** (2025) 054010 (9pp)
https://cstr.cn/32219.14.2058-6272/add9d9
https://doi.org/10.1088/2058-6272/add9d9

Application of a high-speed imaging system for characterization of a hypersonic plasma jet

Changjun LI (李长君), **Qingqing SHU** (舒青青), **Zhiqiang CUI** (崔志强), **Guangyu LI** (李光宇) **and Yong Chia Francis THIO***

Center for Ultimate Energy, ShanghaiTech University, Shanghai 201210, People's Republic of China

*E-mail of corresponding author: zhaoyongzheng@shanghaitech.edu.cn

Received 15 February 2025, revised 16 May 2025
Accepted for publication 16 May 2025
Published 2 June 2025



Abstract

Plasma-jet-driven magneto-inertial fusion (PJMIF), achieving uniform high-Z plasma liners via hypersonic plasma jets ($Ma > 10$), requires precise control of jet reproducibility, synchronization, and mass/velocity uniformity. To address jet nonuniformities in the coaxial plasma gun of the ShanghaiTech Gun1 (STG1) facility, a high-speed imaging system utilizing intensified complementary metal oxide semiconductor (ICMOS) cameras (5120×5120 pixels, 3 ns exposure) with synchronized triggering (< 1 μs delay, < 50 ps jitter) was developed. The system's 45°×45° field of view (42×42 cm^2 midplane coverage) and ~ 1 mm spatial resolution enabled non-perturbative monitoring of hypersonic argon plasma jets (v_{jet} ~ 100 km/s). Triaxial imaging (top/side/end-on views) quantified axial deviations and jet structures, while densitometric profiling derived Mach numbers through boundary spread angles. This diagnostic approach resolves critical challenges in PJMIF gun optimization, with future extensions to multi-channel imaging, narrowband spectral filtering, and 3D reconstruction.

Keywords: PJMIF, coaxial plasma gun, hypersonic plasma jet, high-speed imaging

(Some figures may appear in colour only in the online journal)

1. Introduction

The concept of magneto-inertial fusion (MIF) bridges the parameter space between magnetic confinement fusion (MCF) and inertial confinement fusion (ICF), offering a cost-effective pathway to fusion break-even with reduced research timelines [1–4]. One approach to realize this potential is plasma-jet-driven magneto-inertial fusion (PJMIF) [5–7], which involves the implosion of a magnetized plasma target by a plasma liner. Both the target and the liner are generated by hypersonic plasma jets launched using pulsed coaxial plasma accelerators, also known as Marshall guns [8–10].

To acquire compact, dense, high-velocity, high-Mach-number plasma liners, it is crucial to address the degradation of ram pressure and ensure uniformity in the liners. This necessitates careful consideration of factors such as reproducibility of the plasma guns, synchronization of plasma jet launches, and maintenance of uniformity in jet mass and velocity. Based on 3D modeling studies, it has been determined that variations in jet-to-jet mass and launch timing should be limited to less than 5% and 200 ns, respectively [5, 11]. In addition, single-jet spatial uniformity (e.g., radial density symmetry and axial collimation) required quantitative specifications. These requirements drive the need for advanced diagnostics capable of resolving jet dynamics at millimeter and nanosecond scales.

In this study, we tried to address this challenge through a high-speed imaging system integrated into ShanghaiTech Gun1 (STG1) [12]. Utilizing three orthogonally aligned

* Author to whom any correspondence should be addressed.

All rights, including for text and data mining, AI training, and similar technologies, are reserved.

intensified complementary metal oxide semiconductor (ICMOS) cameras, the system simultaneously captures top, side, and end-on views of argon plasma jets (v_{jet} ~ 100 km/s). Key features include: (1) ultrafast temporal resolution (3 ns exposure) to "freeze" hypersonic jet motion; (2) multi-axis spatial calibration enabling axial deviation quantification (< 1 mm precision); and (3) non-perturbative estimation of jet boundaries and Mach number via densitometric profiling. This diagnostic platform not only qualifies plasma guns during mass production but also informs data-driven optimization of PJMIF liner uniformity, which is a prerequisite for scalable fusion gains [11, 13, 14].

2. Experimental setup

The experimental investigations were conducted using the STG1 experimental facility. A hypersonic plasma jet of argon (Ar, purity > 99.999%) was generated by a coaxial plasma gun system. The typical temperature of the plasma jet was below 2 eV [15], with a total particle density of approximately 10^{16}–10^{17} cm^{-3} [16, 17]. The background vacuum environment ranged from 10^{-3} to 10^{-4} Pa [18]. The velocity of the jet reached approximately 100 km/s, corresponding to a Mach number (*Ma*) exceeding 10.

To quantify and rectify the jet-to-jet nonuniformities of the plasma gun, a key diagnostic system comprising ICMOS cameras was deployed. Three cameras were strategically positioned around the cylindrical experimental vacuum chamber of STG1, as illustrated in figure 1. These cameras could be triggered either by a digital delay generator (DG645) or a photodiode array (PDA), exhibiting a system delay of approximately 1 μs and a jitter in the order of tens of picoseconds. A Cartesian coordinate system was established with its origin at the center of the plasma gun muzzle. The *z*-axis was aligned with the axis of the cylindrical vacuum chamber, with the positive direction corresponding to the jet propagation. The *x*- and *y*-axes were orthogonal to the *z*-axis, with the *x*-axis oriented horizontally and the *y*-axis vertically.

The ICMOS cameras were positioned along the three principal axes as follows: ICMOS camera 1 (port 4) was aligned with the *y*-axis, ICMOS camera 2 (port 8) was aligned with the *x*-axis, and ICMOS camera 3 (port 7) was aligned with the *z*-axis. All cameras were equipped with commercial-grade lenses and focused on the central observation panel through K9 optical glass windows.

In addition to the camera system, a PDA consisting of four individual photodiodes was installed at port 12 of the STG1 chamber. The PDA system configuration included a set of collimators positioned at 55 mm intervals along the *z*-axis, with the first collimator located 225 mm downstream from the muzzle. The collimators collected optical emission signals from the plasma jet with a spatial resolution of approximately 6 mm. The optical signals were transferred via optical fibers to the photodiodes in the screening room through a copper waveguide tube. The first photodiode (z = 225) was connected to DG645 (1 MΩ resistance). The trigger timing could be precisely adjusted by modifying the threshold settings of DG645. The trigger signal was transmitted to the cameras via RG58 coaxial cables. Accounting for the signal delays in the cables (~ 167 ns), DG645 (~ 87 ns), and the camera system (~ 80 ns), the total trigger system delay was calculated to be 0.334 μs. These delay measurements were obtained using a high-performance oscilloscope (Tektronix, 500 MHz bandwidth, 2.5 GS/s sampling rate).

3. Technical features of the ICMOS cameras and spatial calibration

The hypersonic plasma jet studied in this work exhibits an ultrafast velocity (v_{jet}) of approximately 100 km/s. To

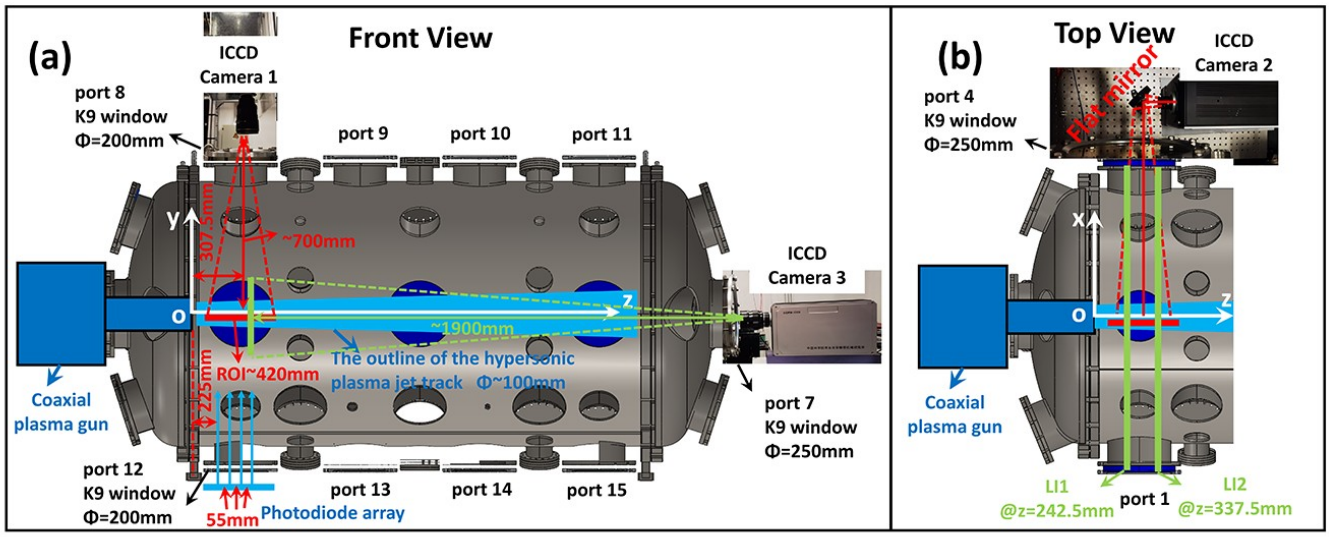


Figure 1. The experimental setup showing (a) STG1 layout equipped with ICMOS cameras (Nos. 1 and 3), PDA detector (front view) and (b) ICMOS camera No. 2 (top view).

resolve the fine structure of the plasma jet, it is imperative to freeze the motion using an extremely short integration time (t_{int}), typically on the nanosecond scale. The state-of-the-art solution for achieving such short t_{int} is through the utilization of an image intensifier coupled with an ultra-high-speed electronic shutter [17, 19, 20]. This configuration enables a rise time of 100–200 ps, facilitating the establishment of a uniform electric field at the photocathode. Additionally, the image intensifier provides appreciable amplification of the optical emission signal between the input signal wavelengths (λ_1 to λ_2) incident on the photocathode and the output light wavelength (λ_{o}) emitted from the luminescent screen. The intensity of output signal on the luminescent screen can be estimated using the following equation:

$$I_{\lambda_{\mathrm{o}}} = \sigma^n \cdot V \cdot \eta_2 \int_{\lambda_1}^{\lambda_2} I(\lambda) \cdot \eta_1(\lambda)\,\mathrm{d}\lambda. \tag{1}$$

Where η_1 is the quantum efficiency of the photocathode and σ is the secondary emission coefficient of the channel material in the microchannel plate (MCP). n represents the number of times electrons strike the inner wall of the MCP during their transit and V is the acceleration voltage between the photocathode and the luminescent screen. Finally, the luminescent screen converts the electrons into photons with a known efficiency (dependent on the type of luminescent screen), denoted by η_2.

The emitted light signal at a specific wavelength from the luminescent screen decays over time (t_1 to t_2) and is subsequently collected by the CMOS sensor. The resulting signal is read out as a digital number (DN) within a given dynamic range. This DN can be calculated using the following expression:

$$\mathrm{DN} = \eta_3(\lambda_{\mathrm{o}}) S \int_{t_1}^{t_2} I_{\lambda_{\mathrm{o}}}(t)\,\mathrm{d}t. \tag{2}$$

Where η_3 is the quantum efficiency of CMOS and S is the internal calibration coefficient of CMOS.

3.1. Technical features

In this study, three identical ICMOS cameras were utilized, all sourced from the same manufacturer, Xi'an Institute of Optics and Precision Mechanics of CAS. These cameras feature image intensifiers with Hot-S20 photocathodes with a gain ranging from approximately 10^3 to 10^4 photons/photon and possess a resolution of 5120×5120 pixels with a pixel size of 2.5 μm. Due to limited spatial resolution of the entire optical system, pixel binning was employed on the cameras. The resolution of the displaced images in this work is 2560×2560 pixels. The spectral response range of the ICMOS cameras spans from 350 to 900 nm. They were deployed on STG1 from ports 8, 4, and 7, and designated as ICMOS cameras 1, 2, and 3, respectively, as shown in figure 1. To accommodate the varying window size and object distance, each ICMOS camera was equipped with a different commercial achromatic lens with focal lengths of 25 mm (ICMOS camera 1), 25 mm (ICMOS camera 2), and 85 mm (ICMOS camera 3). The key technical specifications of the ICMOS cameras are summarized in table 1.

Control of the image intensifier and complementary metal oxide semiconductor (CMOS) sensor is managed by an ultrafast electronics module with an accuracy of better than 1 ns and a jitter of several tens of picoseconds [21]. However, it is important to note that the hardware delays of the image intensifier and CMOS sensor are 80 ns and 2.7 μs respectively. Consequently, the CMOS sensor must receive an arming signal at least 2.7 μs in advance of the entire system being triggered. This presents a critical consideration during system design and implementation. Due to the uncertainty associated with the trigger signal of the PDA during the current development stage at STG1, the CMOS sensor is typically armed approximately 100 μs in advance, with an integration time of 100 ms, ensuring that all signals from the image intensifier can be acquired effectively.

3.2. Spatial calibration

To ensure accurate further application and matrix calculation of camera data, it is imperative to accurately describe the camera viewing geometry. Therefore, in-vessel calibrations were conducted in STG1 to ascertain the direction of the z-axis, spatial resolution, size of the field of view, and any potential spherical aberrations. In this work, the direct linear transformation (DLT) method is employed for calibration [22]. This method allows for the transformation of object-space coordinates to image plane coordinates and enables the parameterization of the line of sight for each pixel as a vector equation. By employing the DLT method, precise calibration of the camera viewing geometry can be achieved, facilitating accurate interpretation and analysis of the acquired data. Figure 2(a) illustrates the positioning of the projection center (N) at coordinates (x_0, y_0, z_0) in object-space and (u_0, v_0, d) in image plane coordinates, respectively. The principal point ($P(u_0, v_0, d)$) on the image plane is determined by projecting a line from N along the axis w (camera direction) perpendicular to the image plane. Notably, since point N, as well as point $O(x, y, z)$ in object space and its projection on the image plane $I(u, v, 0)$, are collinear, the vectors $\overrightarrow{NI} = [u-u_0, v-v_0, -d]$ and $\overrightarrow{NO} = [x-x_0, y-y_0, z-z_0]$ can be effectively equivalent to the vector expression

Table 1. Main technical specifications of the ICMOS cameras.

Feature	Value
Gate width	3 ns–5 s
Jitter	50 ps
Wavelength range	350–900 nm
Size of photocathode	Φ = 18 mm
Luminescent screen	P46
Gain	> 2500 photons/photon
Spatial resolution	> 25 lp/mm
Bit depth	12 bits
Resolution	5120×5120 pixels
Pixel size	2.5 μm

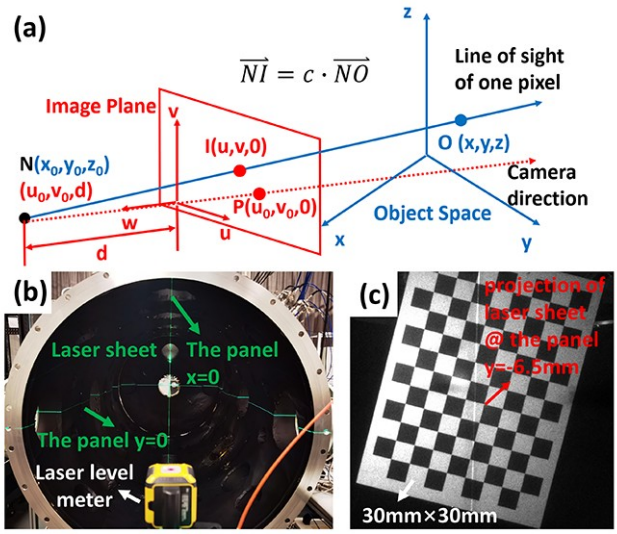


Figure 2. (a) The geometry of projection center (*N*), image panel (*u*, *v*, 0), and object space (*x*, *y*, *z*), (b) in-vessel calibrations in the vacuum chamber of STG1, (c) the image of calibration checkerboard with the projection of laser sheet.

of $\overrightarrow{NI} = c \cdot \overrightarrow{NO}$ (where c is a scaling coefficient). Thus, one can formulate a transformation matrix from object space to the image plane as follows:

$$\begin{bmatrix} u-u_0 \\ v-v_0 \\ -d \end{bmatrix} = c \begin{bmatrix} r_{11} & r_{12} & r_{13} \\ r_{21} & r_{22} & r_{23} \\ r_{31} & r_{32} & r_{33} \end{bmatrix} \begin{bmatrix} x-x_0 \\ y-y_0 \\ z-z_0 \end{bmatrix}. \tag{3}$$

If we introduce unit conversion factors λ_u and λ_v to establish a connection between the units in the digitization system and the image plane coordinates of the real world, we can modify the expressions for $u-u_0$ and $v-v_0$ in equation (3) to $\lambda_u(u-u_0)$ and $\lambda_v(v-v_0)$. Subsequently, we can derive the following relations from equation (3):

$$u-u_0 = -\frac{d}{\lambda_u}\frac{r_{11}(x-x_0)+r_{12}(y-y_0)+r_{13}(z-z_0)}{r_{31}(x-x_0)+r_{32}(y-y_0)+r_{33}(z-z_0)},$$

$$v-v_0 = -\frac{d}{\lambda_u}\frac{r_{21}(x-x_0)+r_{22}(y-y_0)+r_{23}(z-z_0)}{r_{31}(x-x_0)+r_{32}(y-y_0)+r_{33}(z-z_0)}. \tag{4}$$

As a consequence, once a camera system is fixed and established, all mapping relationships are determined. Equation (4) can then be rearranged to solve as follows:

$$u = \frac{L_1x+L_2y+L_3z+L_4}{L_9x+L_{10}y+L_{11}z+1},$$

$$v = \frac{L_5x+L_6y+L_7z+L_8}{L_9x+L_{10}y+L_{11}z+1}. \tag{5}$$

Where L_1–L_{11} represent parameters reflecting the relationships between the object space and image plane. Each time a point (x, y, z) is measured in the object space, a corresponding point (u, v) in the image can be identified, resulting in the acquisition of two equations as described in equation (5). Thus, to solve for the 11 parameters (L_1–L_{11}), at least 6 points (not co-planar) need to be measured. However, given that our camera system comprises over 2.6×10^7 pixels, the equations are easily over-determined. Consequently, the least square method can be employed. It should be noted that optical distortion is not a significant issue in our system, as illustrated in figure 2(c). For the sake of simplicity, optical errors are not considered at the present stage.

The subsequent step involves determining a method to measure points in the object space and their projections in the image plane. Spatial calibration is facilitated by a laser level meter, as depicted in figure 2(b). The horizontal and vertical laser sheets are precisely aligned to coincide with the midplane ($x = 0$ and $y = 0$) of the chamber with an accuracy of approximately 1 mm (equivalent to the thickness of the laser sheet). Subsequently, based on the coordinate system outlined in section 2, every point on the calibration checkerboard (12×9 black and white squares with dimensions of 30 mm) can be defined. The checkerboard is adjusted to be horizontal with an accuracy of ±1 degree, and the x- and z-axes on the checkerboard can be determined with the aid of the laser level meter via the projection of the laser sheet, as shown in figure 2(c). The y-coordinate can be defined by measuring the difference in height between the checkerboard panel and the mid panel. At least two different panels need to be measured to ensure that the control points are not co-planar, and at least two plane calibrations should be conducted. By inputting the control points and employing the aforementioned method, ICMOS camera 1 can be calibrated. Figure 3 illustrates the projection of the image panel onto the object space at different y-values for camera 1. The image has been rotated to align the horizontal and vertical directions with the z- and x-axes, respectively. The imaging reveals that the camera exhibits several millimeters of offset deviation from the center of port 8, which is deemed normal and acceptable.

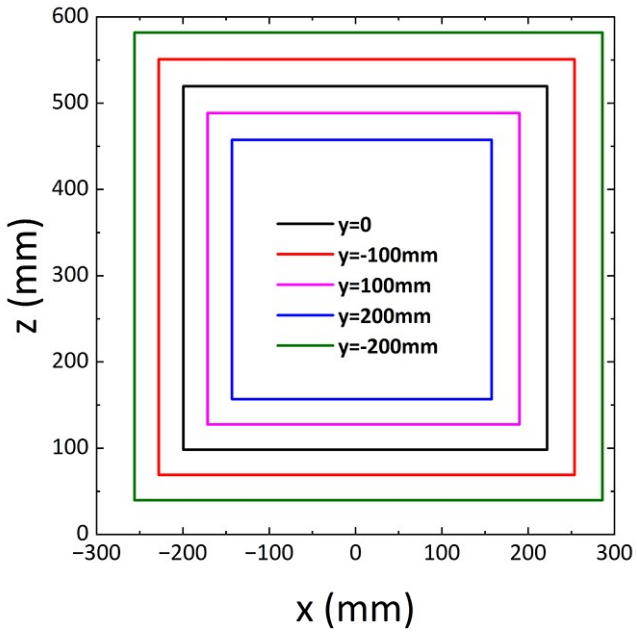


Figure 3. The projection size of the image panel (*xoy* panel) to the object space at different *y*.

4. Application

The optimized experimental configuration with precision spatial calibration achieves high temporal-spatial resolution (1 mm spatial resolution, ns-level delay with ps jitter), enabling advanced diagnostic capabilities for ultrafast plasma phenomena. While the system development remains in its preliminary phase, we have successfully demonstrated several critical applications as outlined below.

4.1. Pre-ionization plasma characterization

In the STG1 plasma acceleration scheme employing slab mode, the dynamic formation of initial gas slabs via ultrafast gas valve injection [18, 23] requires precise temporal control of pre-ionization. This process converts the neutral gas slab into conductive plasma slab to generate compact, high-density collisional plasma. A key optimization parameter is the determination of the minimum temporal window required for achieving azimuthal uniformity in the pre-ionization plasma — particularly crucial given the continuous gas density decay during diffusion between the coaxial electrodes. Premature current initiation risks electrode arcing due to localized current channels, while excessive delay compromises plasma density.

To monitor this critical phase, we employ a gated ICMOS system with 7 μs integration time. The time-resolved imaging sequence in figure 4 reveals the pre-ionization evolution between coaxial electrodes (annotated diameters) over 0–280 μs. The inner and outer diameters of the circular ring represent the inner and outer electrodes of the coaxial plasma gun. The results indicate that the plasma achieves acceptable uniformity within the first ~ 10 μs. Subsequently, over the following ~ 300 μs, negligible uniformity enhancement was found. The pre-ionization plasma exhibits considerable uniformity and symmetry, deemed sufficient for initiating the large current and launching the plasma jet. Notably, there is typically at least one (sometimes two or three) concentrated region (exhibiting strong optical signals) within the pre-ionization plasma at random polar positions. However, no current filamentation was observed during 500 kA level discharges (validated via DDG synchronized 4-channel 8-frame ICMOS imaging), with homogeneous electrode ablation patterns maintained after > 100 shots, both confirming sufficient plasma conductivity and uniformity for stable jet formation without serious damage to the electrode.

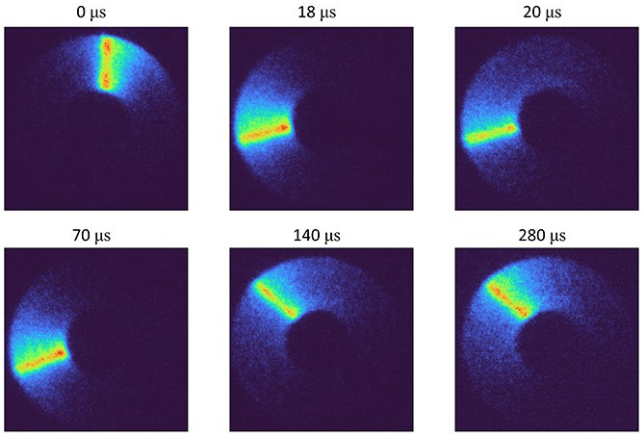


Figure 4. The image (end-on view) of the repeat shots with different time of pre-ionization (gate width = 7 μs, gain = 8000).

4.2. Characterization of the hypersonic plasma jet

Through implementation of black-coated aluminum foil shielding, the suppression of inner wall reflection was achieved. The spatial resolution of the camera (R_c) exceeds 25 line-pairs per millimeter (lp/mm). Considering a total image size (L_{image}) of 12.5 mm representing the length of the field of view (L_{FoV}) of ~ 420 mm, the spatial resolution (R) on the object panel can be calculated using the formula $R = L_{FoV}/R_c/L_{image}$, yielding approximately 1.344 mm.

Jet velocity can be calculated by PDA via comparing characteristic peaks detected by neighboring photodiodes to determine the delay time and their calibrated distance (55 mm) to compute velocity. The typical velocity of 100 km/s requires 13 ns exposure times ($< R/v_{jet}$) for motion artifact suppression. However, an excessively short gate width would be meaningless as the camera cannot distinguish differences smaller than R. Additionally, a low gate width would significantly decrease the signal-to-noise ratio. Considering the possibility of velocities exceeding ~ 130 km/s during the experiment, the integration time is set to be 10 ns.

Figure 5 presents a representative hypersonic jet image

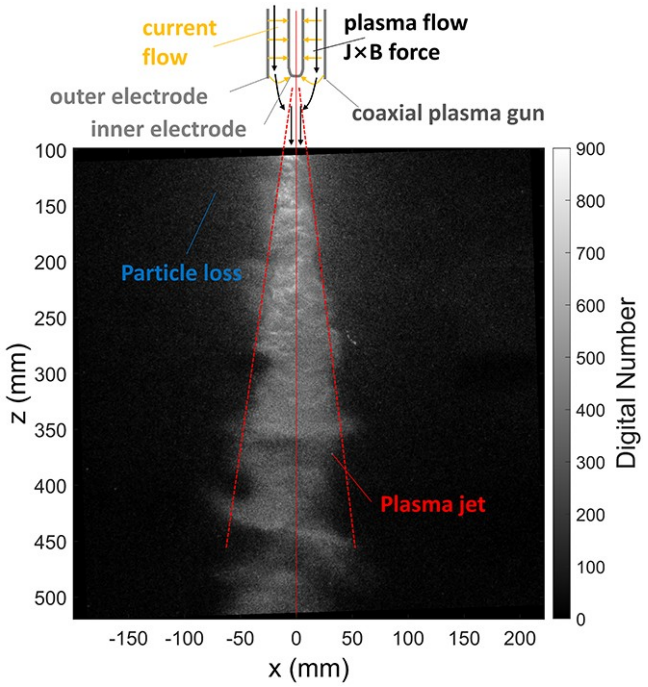


Figure 5. Typical jet image during the STG IOC campaign (20240201 shot 29) at the object panel $y = 0$ from ICMOS camera 1 (top view), delay time = 3.334 μs (triggered by PDA), gate width = 10 ns, gain = 8000.

from the STG1 initial operation capability (IOC) experimental campaign, showing well-constrained z-axis propagation with angular deflection < 0.5 degree. The observed collimation confirms effective $\boldsymbol{J}\times\boldsymbol{B}$ acceleration mechanics at the muzzle exit — a critical validation of the coaxial gun design [10, 24–26]. Notably enhanced scattering noise in the upper part of image suggests Rayleigh scattering interactions with the cloud of particles due to residual chamber gas, uncontrolled neutral particles, and possible edge plasma instabilities. Further investigation is required to address deviations in the jet direction. Apart from potential misalignment of the gun installation with the chamber, the jet direction exhibits slight and random deviations from the z-axis. Due to the same triggering time (triggered by PDA) and quasi-symmetry of the plasma jet, the jet in figure 6(a) shows a high degree of consistency and relevance. On the other hand, the image in figure 6(b) shows a rough directionality in the end-on view. ICMOS camera 3 is equipped with a lens with a relatively longer focal length (85 mm, f/1.2), resulting in a poorer depth of field (estimated to be several cm). Nevertheless, the three cameras positioned in three orthogonal directions still show high potential for multi-view reconstruction feasibility.

4.3. Identification of the plasma boundary and spread angle

The hypersonic plasma jet undergoes radial expansion during propagation, with its expansion velocity (v_{L}) governed by the adiabatic exponent (γ) and temperature. The relationship between v_{L}, γ, and the sound speed of the plasma (c_0) is expressed as [17, 27]:

$$v_{\mathrm{L}} = \frac{2c_0}{(\gamma-1)}. \tag{6}$$

Therefore, it is imperative to identify the boundaries of the plasma jet track, as it contains crucial physical information. In this study, we segmented the jet into slices along the x-direction and characterized the boundary of the plasma jet to parameterize it in high-speed imaging. Figure 7 illustrates the densitometric profiling along the x-axis, which was fitted to a Gaussian function:

$$\mathrm{DN} = C_1 + \frac{C_2}{C_3\sqrt{\pi/2}}\mathrm{e}^{-2\frac{(x-C_4)^2}{C_3{}^2}}. \tag{7}$$

Where C_1–C_4 represent the fitting coefficients. By regressing the camera DN data to equation (7), the full width at half maximum (FWHM) of the Gaussian profile was used to define the plasma boundary. Figures 7(b)–(f) depict the densitometric profiling of five regions of interest (ROI) at different z-positions within a range of 10 mm. Most of the profiling exhibits a Gaussian distribution of the plasma jet, except for figure 7(d), which displays a hollow structure likely caused by the coaxial gun's intrinsic geometry. Despite the dense hypersonic jet ($v_{\mathrm{L}} \ll v_{\mathrm{jet}}$), the steep density gradient at the boundary allows reliable identification via Gaussian fitting, even with localized hollow features.

In figure 7(a), the simulated boundary is marked by red (left), blue (center), and green (right) points. Linear regression of these boundaries shown in figure 8 yielded three linear equations ($x = kz + a$), from which the divergence angle (θ) was calculated using: $\tan\theta = |(k_1 - k_2)/(1 + k_1 \cdot k_2)|$ (θ in figure 8 is ~ 2.37 degrees). v_{L} was then derived as $v_{\mathrm{L}} = v_{\mathrm{jet}} \cdot \tan\theta$, where v_{jet} was obtained from PDA measurements. The Mach number $Ma = v_{\mathrm{jet}}/c_0$, which is a critical parameter for fusion applications, could be estimated by the equation $Ma = 2/[\tan\theta(\gamma-1)]$ [28].

4.4. Comparative analysis with time-resolved laser interferometric measurement (LI)

The STG1 experimental setup employs a two-channel quadrature-heterodyne interferometer (532 nm CW laser, 300 mW output, 10 m coherence length) for time-resolved density characterization of argon hypersonic jets, with the

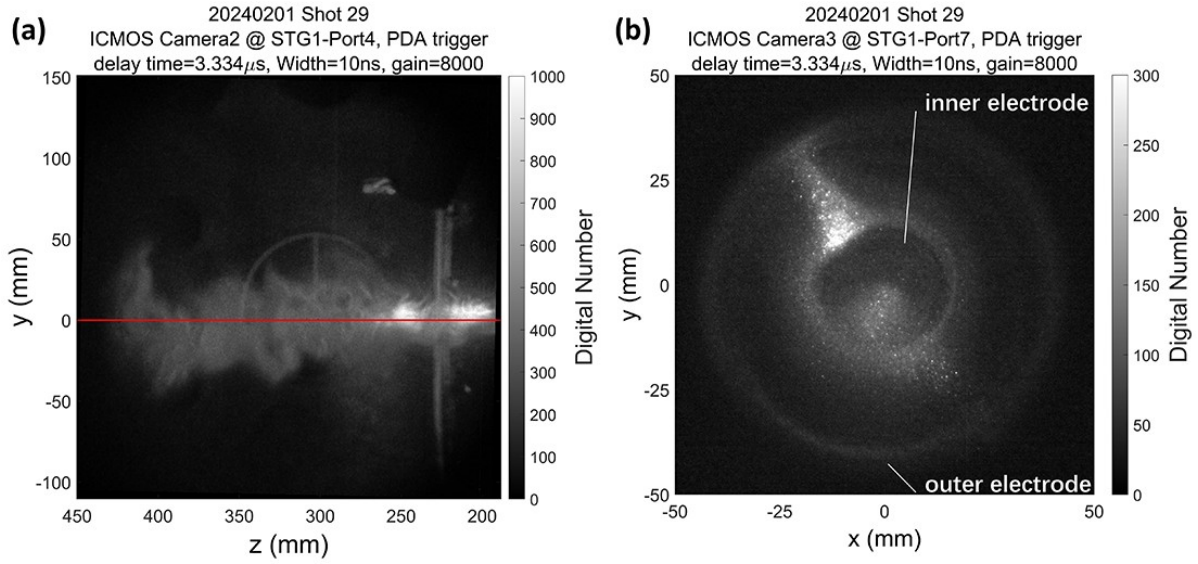


Figure 6. Typical jet image during the STG IOC campaign (20240201 shot 29) from (a) ICMOS camera 2 (front view) and (a) ICMOS camera 3 (end-on view).

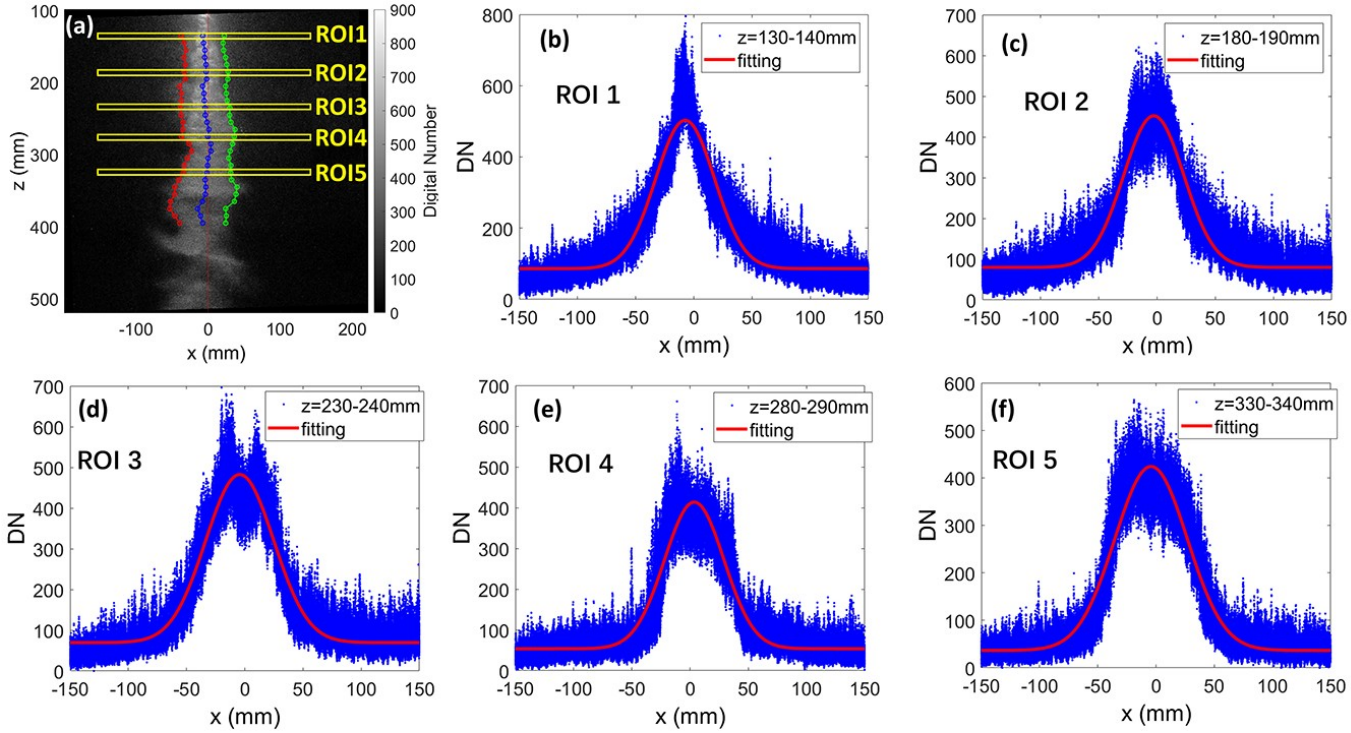


Figure 7. (a) Typical jet boundary shape of a shot in figure 5 and its densitometric profiling along the x-direction in (b) ROI 1: z = 130–140 mm; (c) ROI 2: z = 180–190 mm; (d) ROI 3: z = 230–240 mm; (e) ROI 4: z = 280–290 mm; (f) ROI 5: z = 330–340 mm.

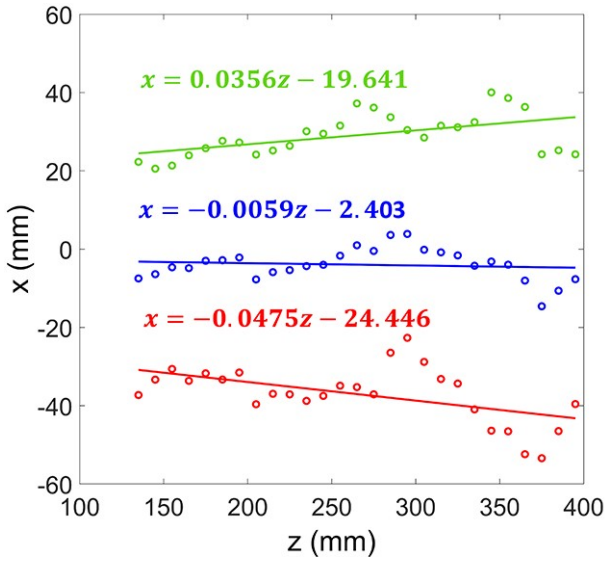


Figure 8. An example of jet boundary identification: red, blue, and green circles (raw data) and lines (fitting boundary) are the left, center, and right boundaries of jet of the typical shot in figure 5 (top view).

diagnostic configuration illustrated in figure 1(b) [16, 29]. The ICMOS camera detects optical emission signals that correlate strongly with plasma temperature and density. For hypersonic plasma jets ($v_{\text{jet}} \gg c_0$), the electron temperature (T_e) can be reasonably assumed to be constant within short muzzle distances (< 1 m). This assumption permits treatment of sound speed, adiabatic exponent (γ), and ion/electron concentrations as constant parameters. Under these conditions, the integrated optical emission from Ar atoms and ions becomes approximately proportional to particle density, reflecting the phase shift observed in line-integrated LI signals. The comparative analysis between camera data and LI measurements serves dual purposes: (1) validates the credibility of the camera signals (ensuring minimal influence from electromagnetic interference) and (2) demonstrates the feasibility of extending LI measurement principles to reconstruct 2D spatial distributions of plasma density.

A fundamental methodological distinction exists between the two techniques. While the camera provides spatially resolved 2D snapshots at discrete time points, LI offers continuous time-resolved data at a single line-of-sight. Effective integration of these complementary methods requires precise synchronization of temporal axes and implementation of space-time transformations. Critical considerations for this synchronization include (1) system-specific delays (positive time shift Δt_1), such as signal propagation delays from the detector to the data acquisition system (DAQ) (cable transmission and DAQ hardware delay); and (2) optical path compensation (negative time shift Δt_2), including light transport delays (e.g., fiber optic transmission) and detector response latency. The net temporal offset is given by $\Delta t_{\text{tot}} = \Delta t_1 - \Delta t_2$. For direct comparison of camera data with line-integrated LI measurements at position z_1 (the chord of LI is orthogonal to z-axis and z_1 = 242.5 mm as shown in figure 1(b)), spatial coordinates along the camera's z-axis must be converted to temporal equivalents using: $\Delta t_{\text{camera}} = (z - z_1)/v_1(t)$, where $v_1(t)$ represents the plasma velocity at position z_1 and time t, obtainable through PDA [16, 30].

Figure 9 demonstrates the strong correlation between the normalized intensity profiles from the camera and LI chord

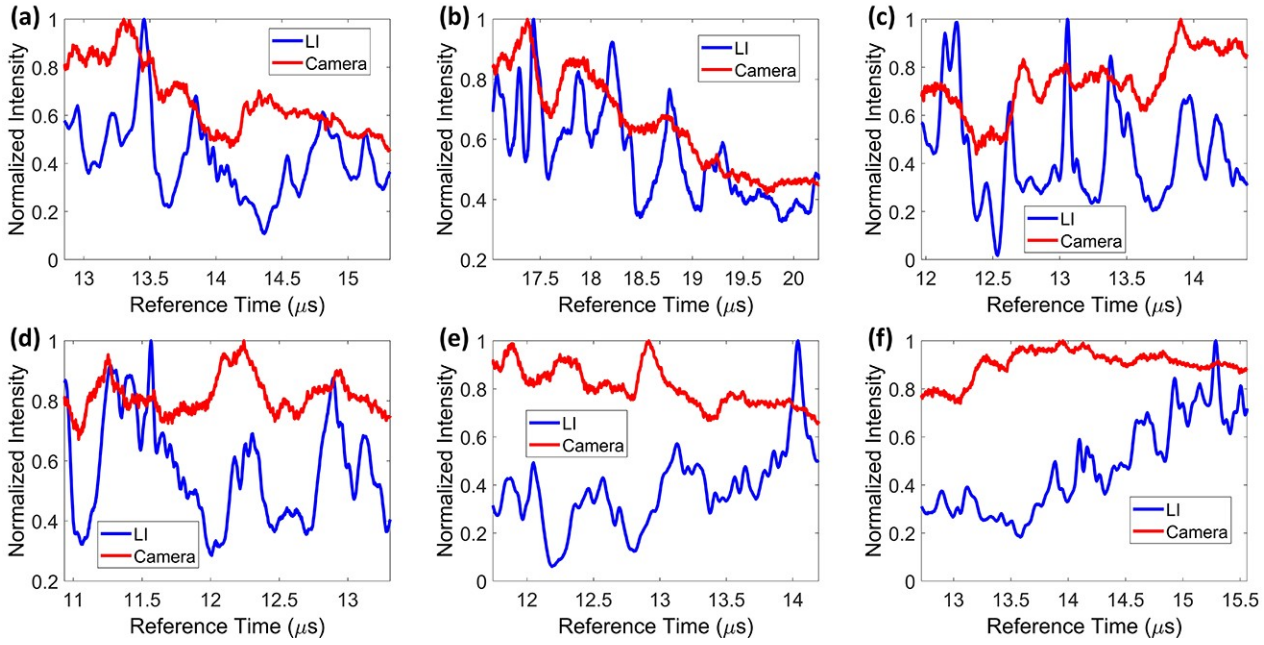


Figure 9. The result of comparison between the camera and LI (normalized) of: (a) 20240201 shot 3; (b) 20240201 shot 6; (c) 20240201 shot 15; (d) 20240201 shot 27; (e) 20240201 shot 29; and (f) 20240201 shot 37.

measurements. This consistency supports the validity of the ICMOS as a reliable diagnostic tool for plasma characterization and confirms measurement fidelity to actual physical conditions.

5. Summary

The deployment of a high-speed imaging system, comprising three ICMOS cameras, at STG1 has been instrumental in characterizing a hypersonic plasma jet. Through this work, three main applications were demonstrated: (i) characterizing pre-ionization plasma between coaxial electrodes; (ii) characterizing the hypersonic plasma jet with a nanosecond scale integration time; and (iii) precise determination of plasma boundary morphology and spread angle. The system's extremely short integration time of 3 ns, coupled with an ultrafast electronics module boasting an accuracy of better than 1 ns and a jitter of several tens of ps, permits "freeze-frame" capture of hypersonic plasma jets with exceptional reproducibility. Additionally, its high spatial resolution of approximately 1 mm at a distance of approximately 700 mm allows for the imaging of plasma fine structure and accurate boundary identification. Cross-validation with laser interferometric (LI) measurements confirms both the temporal fidelity and electromagnetic interference immunity of the camera signals, while simultaneously demonstrating the feasibility of extending LI principles to 2D spatial reconstructions. As a result, the high-speed imaging system has effectively addressed critical challenges associated with coaxial plasma guns by providing precise diagnostics of jet-to-jet nonuniformities, axial deviations, and jet structures.

While these achievements represent significant progress, continued development of the imaging system remains imperative for comprehensive plasma physics analysis and optimized plasma gun design in PJMIF applications. Strategic enhancements could include (1) multi-spectral imaging through narrow bandpass filter integration [31], (2) expanded channel capacity for more frames in one single shot, and (3) implementation of stereoscopic 3D reconstruction techniques for advanced tomographic analysis of plasma distributions.

Acknowledgments

This work was supported by the Major National Science and Technology Infrastructure (No. 2208-000000-04-01-249628).

References

[1] Lindemuth I R and Kirkpatrick R C 1983 *Nucl. Fusion* **23** 263
[2] Hsu S C and Langendorf S J 2018 *J. Fusion Energy* **38** 182
[3] Knapp C E and Kirkpatrick R C 2014 *Phys. Plasmas* **21** 070701
[4] Yager-Elorriaga D A *et al* 2022 *Nucl. Fusion* **62** 042015
[5] Thio Y C F *et al* 2019 *Fusion Sci. Technol.* **75** 581
[6] Yates K C *et al* 2020 *Phys. Plasmas* **27** 062706
[7] Langendorf S J *et al* 2019 *Phys. Plasmas* **26** 082110
[8] Hsu S C *et al* 2012 *IEEE Trans. Plasma Sci.* **40** 1287
[9] Thoma C *et al* 2011 *Phys. Plasmas* **18** 103507
[10] Witherspoon F D *et al* 2009 *Rev. Sci. Instrum.* **80** 083506
[11] Shih W *et al* 2019 *Phys. Plasmas* **26** 032704
[12] Thio Y C F *et al* 2024 A third-generation coaxial plasma gun (STG1) for PJMIF application In: *Proceedings of 2024 IEEE International Conference on Plasma Science* Beijing: IEEE 2024 doi: 10.1109/ICOPS58192.2024.10626893
[13] LaJoie A L *et al* 2023 *Rev. Sci. Instrum.* **94** 063503
[14] Schillo K and Cassibry J 2020 *Phys. Plasmas* **27** 042707

[15] Li M *et al* 2024 Spectroscopic measurement of the electron temperature of a hypersonic plasma jet In: *Proceedings of 2024 IEEE International Conference on Plasma Science* Beijing: IEEE 2024 doi: 10.1109/ICOPS58192.2024.10625801
[16] Li G *et al* 2024 Laser interferometric measurement of the plasma density of hypersonic plasma jets launched by a coaxial plasma gun In: *Proceedings of 2024 IEEE International Conference on Plasma Science* Beijing: IEEE 2024 doi: 10.1109/ICOPS58192.2024.10626383
[17] Hsu S C *et al* 2012 *Phys. Plasmas* **19** 123514
[18] Zhang D *et al* 2024 Development of an ultrafast gas valve in a plasma gun for PJMIF application In: *Proceedings of 2024 IEEE International Conference on Plasma Science* Beijing: IEEE 2024 doi: 10.1109/ICOPS58192.2024.10627655
[19] Moser A L and Hsu S C 2015 *Phys. Plasmas* **22** 055707
[20] Hsu S C *et al* 2018 *IEEE Trans. Plasma Sci.* **46** 1951
[21] Li X *et al* 2024 *Laser Optoelectron. Prog.* **61** 0211020
[22] Meyer W H *et al* 2018 *Rev. Sci. Instrum.* **89** 10K110
[23] Thio Y C F *et al* 2024 A two-stage gas injection system for coaxial plasma gun as a driver for PJMIF In: *Proceedings of 2024 IEEE International Conference on Plasma Science* Beijing: IEEE 2024 doi: 10.1109/ICOPS58192.2024.10627043
[24] Thio Y C F, Cassibry J T and Markusic T E 2002 Pulsed electromagnetic acceleration of plasmas In: *Proceedings of the 38th AIAA Joint Propulsion Conference & Exhibit* Indianapolis: AIAA 2002
[25] Thio Y and Frost L 1986 *IEEE Trans. Magn.* **22** 1757
[26] Baker K L *et al* 2002 *Nucl. Fusion* **42** 94
[27] Thio Y C F, Hao C J and Qi S B 2024 Partition functions, adiabatic exponent and their role in the analysis of spectroscopic Doppler shift in determining the Mach number and temperature of a hypersonic plasma jet In: *Proceedings of 2024 IEEE International Conference on Plasma Science* Beijing: IEEE 2024 doi: 10.1109/ICOPS58192.2024.10627014
[28] Cassibry J T, Thio Y C F and Wu S T 2006 *Phys. Plasmas* **13** 053101
[29] Case A *et al* 2010 *Phys. Plasmas* **17** 053503
[30] Sun Y *et al* 2024 Development of a laser interferometric system for measuring the density of a hypersonic plasma jet In: *Proceedings of 2024 IEEE International Conference on Plasma Science* Beijing: IEEE doi: 10.1109/ICOPS58192.2024.10626456
[31] Byvank T *et al* 2020 *Phys. Plasmas* **27** 042302